Appl. Phys. A (2016) 122:62
DOI 10.1007/s00339-016-9603-z

Applied Physics A
Materials Science & Processing

CrossMark

Optical and electrical characterization of CIGS thin films grown by electrodeposition route

Chihi Adel[1] · Boujmil Mohamed Fethi[1] · Bessais Brahim[1]

Received: 15 November 2015 / Accepted: 3 January 2016 / Published online: 14 January 2016
© Springer-Verlag Berlin Heidelberg 2016

Abstract In this paper, the electrochemical impedance spectroscopy was handled to study the electrochemical attitude of quaternary alloy Cu (In, Ga) Se_2/Na_2SO_4 electrolyte interface. Subsequently, an annealing treatment was performed at various temperatures (250–400 °C). The material features of Cu (In, Ga) Se_2 films are controlled by the percentage of gallium content. XRD studies showed three favorite orientations along the (112), (220), and (116) planes for all samples. The morphological and chemical composition studies exhibited Ga/(Ga + In) ratio ranging from 0.27 to 0.32, and RMS surface roughness was in the range 54.2–77.8 nm, respectively. The optical band gap energy of the CIGS alloys can be strongly controlled by adjusting gallium and indium concentrations. EIS measurement has been modeled by using an equivalent circuit. Mott–Schottky plot illustrates p-type conductivity of CIGS film with a carrier concentration around 1016 cm^{-3}, a flat band potential V_{fb} ranging from −0.68 to −0.57 V, and depletion layer thickness rises from 0.24 to 0.36 µm.

1 Introduction

Cu (In_{1-x}, Ga_x) Se_2 (CIGS) quaternary alloys are promising semiconductor which have been extensively studied for photovoltaic applications. Currently, CIGS thin film reached conversion efficiency above 21.7 % with a cell area of 0.5 cm^2 [1]. Additionally, CIGS semiconductors have an extraordinary potential for solar energy conversion because of their direct band gap and high absorption coefficient [2]. For requests, CIGS semiconductors have a tunable band gap to be a photoabsorber in solar cells [3]. Till now, several attempts have been employed to produce CIGS films, for example, co-sputtering [4], chemical spray deposition [5], spray pyrolysis [6], ink print techniques [7–9], and electrodeposition [10–12]. Among these techniques, electrodeposition is simple and economical as compared to expensive vacuum treatment processes. However, electrodeposition of quaternary alloys is slightly difficult, because of a great difference in deposition potential of the precursors, and owing to the possibility of the creation of intermediate phases throughout electrodeposition.

It is well known that electrochemical impedance spectroscopy (EIS) is a common approach of investigating electrochemical devices, suitable to different inhomogeneous phenomena such as organic electroluminescence devices and dye-sensitized solar cells for design and decline processes [13, 14]. Among, the convenience of EIS is that it can determine which capacitance and resistance are altered by the presence of defects, grains, and diffusion of atoms. A huge number of alloys have been studied by EIS, for instance, $CoFe_2O_4$ [15], InP [16], In_2S_3 [17], and Mg_2Ni [18]. In Valderrama et al. [19] has been studied CIGS/electrolyte interface (specifically H_2SO_4 electrolyte) by EIS; however, far too small consideration has been paid to understanding the influence of the Ga/(Ga + In) ratio on p-CIGS alloy/Na_2SO_4 electrolyte interface. Thus, applying EIS to investigate CIGS solar cells is promising tool to study CIGS/Na_2SO_4 electrolyte interface. Indeed, many intricate phenomena that impact the performance of solar cells were observed around the CIGS/Na_2SO_4 electrolyte interface such as the frequency dispersion of the

✉ Chihi Adel
supereagle2791@yahoo.fr

[1] Laboratory of Photovoltaic, Centre of Research and Technology of Energy, Technopole of Borj Cedria, B.P No 95, 2050 Hammam Lif, Tunisia

capacitance of the $CIGS/Na_2SO_4$ interface. This phenomenon reliably confuses the analysis of the data and the dedication of flat band potential.

In this present work, we examine the influence of Ga/(In + Ga) ratios in an acidic solution bath on physical proprieties, and stability of the potentiostatically deposited CIGS alloys onto conductive glass ITO substrates. In addition, correlating the impedance spectra with their underlying microstructure in order to find an appropriate equivalent circuit.

2 Experiment

CIGS alloys deposited on conductive glass ITO substrates with 100 nm thickness, sheet resistance about 20 Ω sq^{-1}, and the transmission in the visible range of the spectrum were beyond 90 % by a deposition technique using a standard three-electrode system. At the first step, the ITO-coated glass substrates were cut into several pieces (2.0 × 2.0 cm^2), and cleaned ultrasonically with acetone, isopropanol, distilled water for 10 min, and placed in drying oven for 30 min. The deposition process was accomplished by using a standard three-electrode system. The solution bath, which contained the precursors of the CIGS material, i.e., 12 mM $CuCl_2$ (Sigma-Aldrich 99.995 %) for copper, 2.5–3.6 mM $InCl_3$ (Sigma-Aldrich 99 %) for indium, 0.4–1.6 mM $GaCl_3$ (Sigma-Aldrich 99.995 %), 25 mM SeO_2 (Sigma-Aldrich 99.9 %), 25 mM sulfamic acid which can inhibit the underpotential deposition of Cu_2Se phases and the H^+ reduction into H_2 which are considered as the undesired process [20], and 0.1 M trisodium citrate ($Na_3C_6H_5O_7$) which was chosen to be a complex agent in the electrolyte [21]. Thereafter, a high-purity dilute HCl (1 M) solution was added drop-by-drop, until the pH reached 1.90–2.10 [22]. All CIGS alloys were deposited using autolab (PGP201) potenciostat/galvanostat controlled with a computer and connected to three electrodes at optimal deposition potential −700 mV versus SCE for 20 min. For all samples, the thickness of CIGS alloys is around 1 µm.

The solution was not altered during deposition and was not deaerated before or during deposition. A thin, dark-blue film was deposed uniform, homogeneous and well adherent to the substrate. Finally, annealing temperature was varied from 250 to 400 °C inside quartz tube furnace under nitrogen during 10–30 min. Following annealing, the tube furnace was cooled to room temperature 25 °C. The structural properties of the annealed CIGS thin films were studied by high-resolution X-ray diffraction using a Bruker D8 advance (both Bragg–Brentano) with CuK_α radiation ($\lambda = 1.5405$ Å) in 2θ values between 10° and 70°.

The surface morphologies of the films were observed by an atomic force microscope (AFM) in tapping configuration to scan an area of (1 × 1 μm^2). The roughness was customized with WSxM software ver. 5.0 [23]. The chemical composition of the CIGS films was determined using energy-dispersive X-ray spectroscopy (EDS). The optical transmittance and reflectance spectra of the thin films were measured by using UV–Visible Perkin Elmer Lambda 950 spectrophotometer in the wavelength ranging from 300 to1500 nm.

The impedance measurement was achieved with a Frequency Response Analyzer (prod.Solatron, Model 1294) coupled to a potentiostat with three-electrode system: CIGS thin film was used as the working electrode, a platinum wire as the counter electrode, SCE as a reference electrode, and 0.5 M Na_2SO_4 as electrolyte. EIS data were performed at room temperature 298 °C and in open-circuit potential. The amplitude of the sinusoidal voltage signal perturbation of 10 mV was applied to the electrodes above the frequency range of 40 Hz–0.3 MHz. The pH of the liquid containing 0.5 M Na_2SO_4 was saved at 7.0. Mott–Schottky plots were performed in the range of 1–0 V (vs. SCE) reference electrode in frequency of 1 kHz.

3 Results and discussion

3.1 Structural characterization

Figure 1 displays the X-ray diffraction patterns of the CIGS thin films annealed at various temperatures ranging from 250 to 400 °C prepared on ITO-coated glass substrates with bath composed of 12 mM $CuCl_2$, 2.8 mM $InCl_3$, 1.2 mM $GaCl_3$, and 25 mM SeO_2. After annealing process, the CIGS thin films exhibit similar diffraction peak around 26.8° and indicate the polycrystalline CIGS

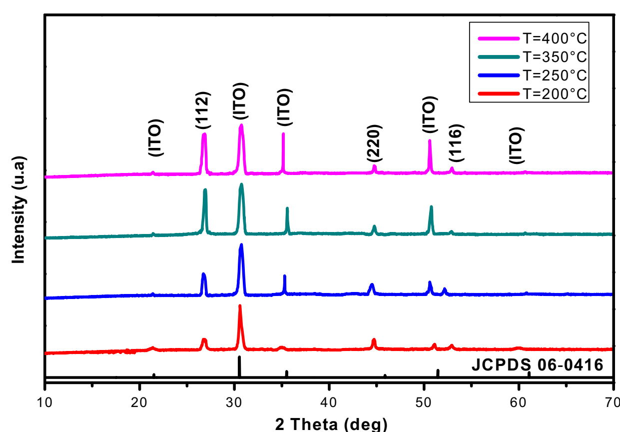

Fig. 1 XRD patterns of CIGS alloys deposited at −700 mV versus SCE for 20 min at various annealing temperatures

phase with a preferential orientation (112) plane, and other well-known peaks correspond to the (220)/(204) and (312)/(116) planes. This was confirmed by JCPDS (Joint Committee on Powder Diffraction Standards) database for CIGS tetragonal chalcopyrite structure with card number (35-1102). In addition, as can be shown from Fig. 1, there are another peaks which correspond to conductive glass ITO substrate (JCPDS 06-0416). By the increase in annealing temperature, diffraction peak intensity of the (112) plane enhanced considerably and reached its maximum value at 350 °C owing to grain growth of the film. The full width at half maximum (FWHM) of (112) plane decreases with annealing temperature. This effect involves that with increase in annealing temperature, the deposit CIGS alloys find better. However, it should be noted that for high temperature above 350 °C, the peak intensity of the (112) plane decreases and FWHM became larger. A similar result was found by Venkatachalam [24].

Thus, this survey keeps the annealing temperature at 350 °C to examine the behind experiments.

3.2 Morphology and stoichiometry analysis

The surface morphologies of deposited films were investigated by atomic force microscopic (AFM). Figure 2 shows micrographs of the CIGS films with various Ga and In concentrations at optimized potential −0.7 V during 20 min and under annealing temperature 350 °C. As the [Ga]/[In] + [Ga] molar ratios increases, the root-mean-square (RMS) surface roughness increases also. This aspect is qualified to the substitution of Ga atoms for In atoms in the CIGS structure, which engenders the decrease in *d*-spacing and satisfies the integration of Ga atoms into the CIS matrix to figure CIGS alloy. The RMS surface roughness values which determined by WSxM software are listed in Table 1. From this study, it can be provided that the surface roughness of deposit films was mainly influenced by the [Ga]/[In] + [Ga] molar ratios.

On the other hand, the chemical composition of the CIGS alloys was achieved by using EDS data and the ratio of Ga/(Ga + In) in the CIGS films was calculated. Table 2 illustrates the detailed at.% of Cu, In, Ga, and Se. EDS measurement shows that the percentage composition of Ga content increases as the ratio of Ga/(Ga + In) increases. Furthermore, when the [Ga]/[In] + [Ga] is equal to 0.3, the EDS analysis reveals an average elemental composition of 20.57 at.% Cu, 14.53 at.% In, 6.25 at.% Ga, and 39.19 at.% Se, completely corresponding to the ultimate alloy composition of Cu ($In_{0.7}$, $Ga_{0.3}$) Se_2. These results are consistent with X-ray diffraction analysis mentioned

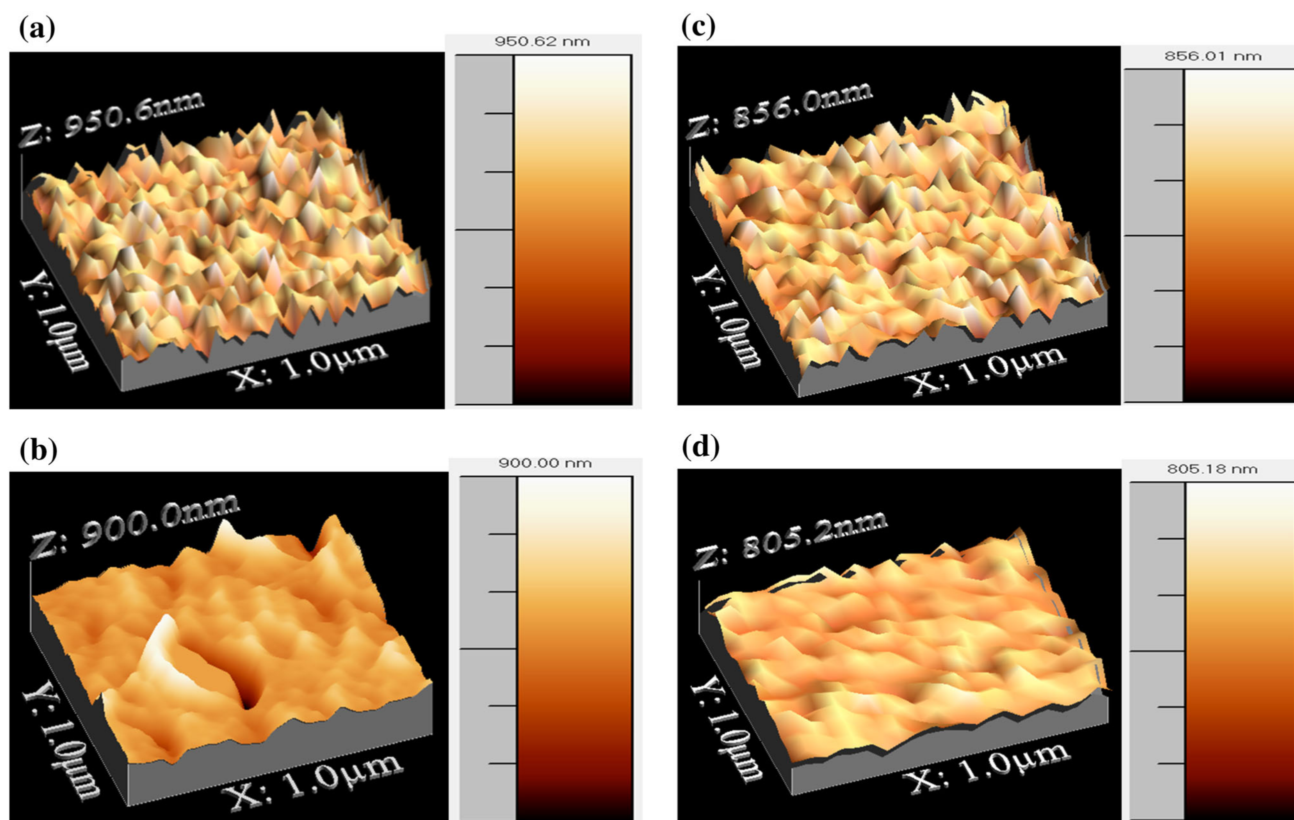

Fig. 2 AFM micrographs of CIGS alloys with different gallium and indium concentrations. $x = 0.1$ (**a**), $x = 0.2$ (**b**), $x = 0.3$ (**c**), $x = 0.4$ (**d**)

Table 1 RMS surface roughness determined by atomic force microscopy (AFM) for CIGS alloys deposited at optimized potential −700 mV for 20 min at 350 °C

x = [Ga]/[In] + [Ga]	Roughness (nm)
0.1	54.2
0.2	65.5
0.3	71.2
0.4	77.8

above. Hanna et al. [25] suggested that the usual Ga/(Ga + In) ratio is in the bounds of 0.1–0.3 and the defect concentration in CIGS film is less as the Ga/(Ga + In) ratio at about 0.3.

From the above study, the CIGS film deposited at −700 mV during 20 min at annealing temperature 350 °C is suitable in composition to be used as the photoabsorber alloy of photovoltaic devices.

3.3 Optical proprieties

Transmission $T(\lambda)$ and reflection $R(\lambda)$ data are accomplished by using an UV–Vis–NIR spectrophotometer in the range 300–1500 nm for to compare the effect of Ga/(In + Ga) molar ratio on the optical energy band gap of CIGS films. Figure 3 shows the variation in $(\alpha h\nu)^2$ versus $h\nu$ of CIGS films. The optical energy band gap was estimated from $(\alpha h \nu)^2$ versus $h\nu$ plots, and the absorption coefficient (α) for CIGS films was evaluated using the following equation [26]:

$$\alpha = \frac{1}{d}\ln\left[\frac{(1-R)^2}{T}\right] \quad (1)$$

where d is the thickness of CIGS alloys, and $T(\lambda)$ and $R(\lambda)$ are optical transmission and reflectance measurement, respectively. The variation in α with energy ($h\nu$) near the principal absorption edge of optical band gap CIGS film seems forward to well-known Tauc law [27]:

$$(\alpha h\nu)^2 = A\left(h\nu - E_g\right) \quad (2)$$

where A is a constant, E_g is the optical energy band gap, and h ν is the photon incident energy. The optical energy band gap of CIGS films was evaluated by plotting $(\alpha h\nu)^2$ versus $h\nu$ from Eq. (2) and by extrapolating the linear portion of the spectrum $(\alpha h\nu)^2 = h\nu$ to zero.

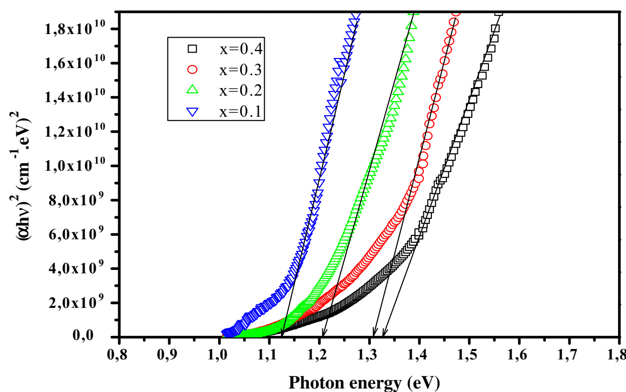

Fig. 3 Band gap estimation for CIGS thin films annealed at 350 °C with various Ga/(In + Ga) ratios

As the Ga/(In +Ga) increases from 0.27 to 0.32, optical energy band gap increases from 1.12 to 1.33 eV. Zhang et al. [28] have deposited CIGS alloys by the three-stage co-evaporation process on glass substrate and the achieved optical band gap is around 1.18 which is consistent with our results. The shift to higher energy of optical band gap may be attributed to variation in surface roughness, which provides the creation of defect states in the optical band gap.

3.4 Impedance studies of CIGS film in 0.5 M Na_2SO_4 solution

Figure 4 exhibits representative Nyquist plots (imaginary impedance (Z'') versus real impedance (Z')) of the CIGS alloys in 0.5 M Na_2SO_4 solution at pH = 7.1 with different Ga/(In + Ga) ratio ranging from 0.27 to 0.32. Clearly, the Nyquist plots reveal one depressed semicircular arcs in the measured frequency ranging from 40 Hz to 0.3 MHz with their diameters changing through varying the Ga/In + Ga ratios. Furthermore, the semicircular arcs their centers are placed below the real axis Z' implying the nonideal contact. The radii of the semicircular arc tend to increase with increasing Ga/(In + Ga) ratio. The only frequency arc denotes restrictive charge

Table 2 Various bath compositions and the corresponding atomic ratio

x = [Ga]/[Ga] + [In]	Bath composition (mM)				Atomic ratio (%)				Ga/(Ga + In)
	Cu	In	Ga	Se	Cu	In	Ga	Se	
0.1	12	3.6	0.4	25	18.23	13.65	5.28	35.90	0.27
0.2	12	3.2	0.8	25	19.87	13.53	5.71	36.09	0.29
0.3	**12**	**2.8**	**1.2**	**25**	**20.57**	**14.53**	**6.25**	**39.19**	**0.30**
0.4	12	2.4	1.6	25	20.33	14.53	7.01	38.69	0.32

Bold values indicate experimental optimum composition for ultimate CIGS solar cell efficiencies

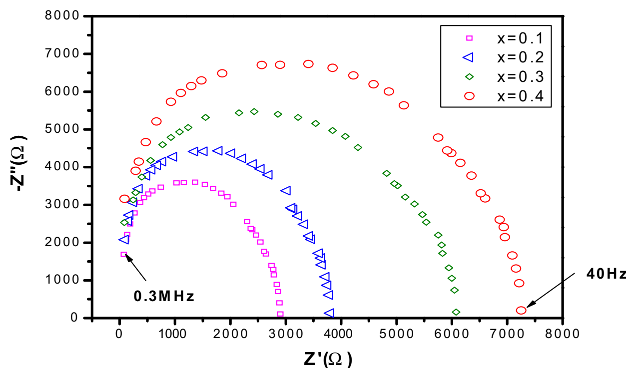

Fig. 4 Nyquist diagrams for CIGS film annealed at 350 °C in 0.5 M Na_2SO_4 in frequency ranging 40 Hz–0.3 MHz at different Ga/(In + Ga) ratios

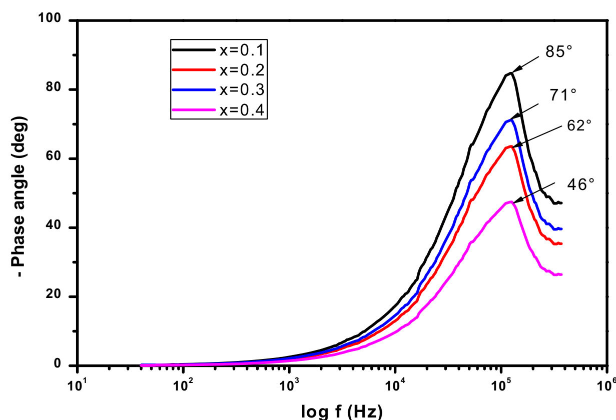

Fig. 5 Phase shift diagrams for CIGS alloys annealed at 350 °C in aqueous solution containing 0.5 M Na_2SO_4 at several Ga/In + Ga ratios ranging from 0.27 to 0.32

transfer and conceivably qualified to double-layer capacitance in parallel with the charge transfer resistance at the junction between CIGS/Na_2SO_4 interface. According to Fig. 5 (phase angle vs. frequency), the phase angle magnitude was affected by varying Ga/(In + Ga) ratio and ranging between 46° and 85°, which is fewer negative than that of an ideal capacitor (90°), representing frequency dispersion. These effects revealed that there are many inhomogeneity phenomena, for example, defects and grain boundaries, around the CIGS/Na_2SO_4 electrolyte interface.

With the intention to explain this behavior, a simple equivalent circuit was well matched with experimental impedance spectroscopic data for CIGS/Na_2SO_4 interface. Figure 6 shows the equivalent circuit well matched with the experimental impedance data to find a satisfactory impedance model of CIGS in Na_2SO_4 solution. It is required to substitute the capacitor C with a constant phase element (CPE) in the equivalent circuit. A constant phase

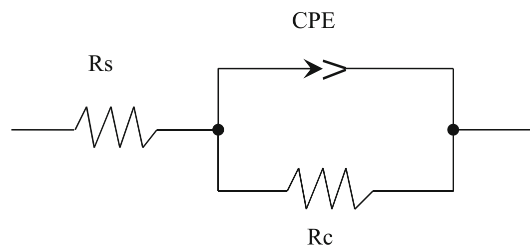

Fig. 6 Randles CPE model circuit appropriate with the experimental impedance data for CIGS electrodes in aqueous solution containing 0.5 M Na_2SO_4

Table 3 Equivalent circuit parameters of CIGS alloys annealed at 350 °C with diverse Ga/(In + Ga) ratios in aqueous solution containing 0.5 M Na_2SO_4

Ga/In + Ga	R_s (Ω)	R_c (Ω)	Q (F cm^{-2} s^{p-1})	p
0.27	72	3056	1.03E−4	0.88
0.29	98	4177	9.13E−5	0.78
0.30	84	6044	4.04E−5	0.73
0.32	86	6842	3.39E−5	0.76

element (CPE) is the impedance that exhibits nonideal capacitor where capacitance varies with frequency. Likewise, nonideal behavior creates from a rough surface with some inhomogeneities [29] and/or dielectric relaxation either in the depletion region or at the CIGS/Na_2SO_4 interface [30, 31]. The impedance Z_{CPE} is described by CPE index "p" (CPE-p) and CPE constant "Q" (CPE-Q) as follows [32]:

$$Z_{CPE} = \left((j\omega)^p Q\right)^{-1} \quad (3)$$

where j represents the imaginary unit, ω the angular frequency, Q a constant independent of frequency in F cm^{-2} s^{n-1} [33], and $0 < p < 1$. When p equal to 1, the CPE is a pure capacitance, and for an ideal resistor, it is 0. Here, R_s is the electrolyte resistance, R_c and CPE double-layer capacitance characterize faradic charge transfer resistance and constant phase element of double layer, respectively.

Table 3 exhibits the equivalent circuit parameters for the impedance spectra of CIGS in different Ga/(In + Ga) ratio ranging from 0.27 to 0.32. Clearly, the electrode and electrolyte resistance R_s rest approximately invariable above the complete series concentrations of Ga and In with the values between 72 and 98 Ω. However, R_c increases and CPE decreases with increasing Ga/In + Ga ratio. The charge transfer resistance R_c for Ga/(In + Ga) equal to 0.27 shows the lowest value, and this means that acquires the highest electron transfer efficiency. And, on the other hand, a rise of CPE response at high frequencies with Ga/(In + Ga) ratio may be due to roughness at the close interface.

To examine the impedance measurement of a CIGS/Na_2SO_4 interface, the Mott–Schottky relation shows an important function. Indeed, we can establish the carrier type, carrier concentration, flat band voltage, Debye screening distance, and depletion width. In this equation, linear relationship is expected between the applied potential and the reciprocal of the square of the depletion region capacitance (CSC), i.e., [34].

$$\frac{1}{C^2} = \left(\frac{2}{\varepsilon\varepsilon_0 e A^2 N}\right)\left(\pm(V - V_{\mathrm{fb}}) - \frac{kT}{e}\right) \tag{4}$$

In which, ε is the dielectric constant of the alloy, ε_o permittivity of a vacuum (8.85×10^{-12} F m^{-1}), e elementary electric charge (1.60×10^{-19} C), k Boltzmann constant (1.38×10^{-23} J K^{-1}), and T absolute temperature (298 K). Besides, A and N denote the surface area of the electrode and the density of donor or acceptor in the semiconductor, respectively. V is the externally applied potential against the SCE electrode, and V_{fb} is the flat band potential. From this relationship, V_{fb} was gathered from V_0, the point of intersection of the V-axis of a C^{-2} versus V plot:

$$V_0 = V_{\mathrm{fb}} + \frac{kT}{e} \tag{5}$$

Furthermore, N_A can be determined whether (ε) and (A) are known. The dielectric constant of CIGS was 13.6 [35], and the area of the interface was taken 1 cm^2 in this work. Negative slope illustrates the p-type conductivity of the CIGS films. Figure 7 shows a quasi-straight line $1/C^2$ versus V and intersecting the voltage axis at the value V_0. From the fit line slope, we can determine N_A. The determined V_{fb} and N_{A} values are presented in Table 4. The expected flat band potentials (V_{fb}) of CIGS films ranged from −0.68 to −0.57 V and became more positive with increasing Ga/(In + Ga) ratio. Carrier densities of CIGS films gathered from the slope of Mott–Schottky plots by using the following relation:

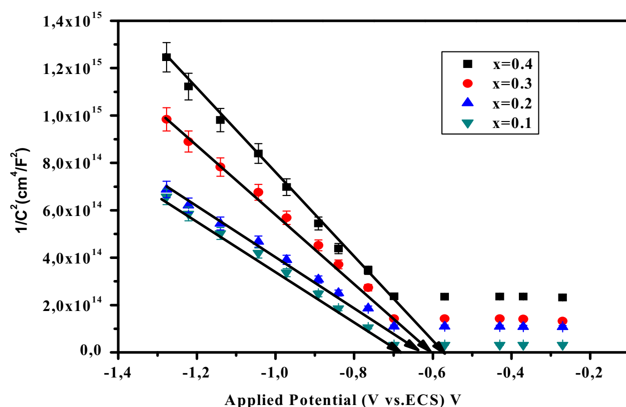

Fig. 7 Mott–Schottky plots ($1/C^2$ vs. V) of CIGS thin film deposited on conductive glass ITO substrates in aqueous solution containing 0.5 M Na_2SO_4

Table 4 Mott–Schottky parameters for CIGS alloys in aqueous solution containing 0.5 M Na_2SO_4 annealed at 350 °C with various Ga/(In + Ga) ratios

Ga/ In + Ga	V_{fb} (V)	Carrier density (cm^{-3})	W_{D} (μm)	L_{D} (μm)
0.27	−0.49	6.49E15	0.36	0.34
0.29	−0.43	8.18E15	0.32	0.15
0.30	−0.52	1.14E16	0.27	0.12
0.32	−0.37	1.42E16	0.24	0.11

$$N_A = \left(\frac{2}{\varepsilon\varepsilon_0 e A^2}\right)\left[\frac{\mathrm{d}\left(\frac{1}{C^2}\right)}{\mathrm{d}V}\right]^{-1} \tag{6}$$

Carrier density ranges from 6.49×10^{15} to 1.42×10^{16} cm^{-3} and rises with increasing Ga/In + Ga ratio. This result is in respectable accord with that reported by Pan et al. [36]. Also, Mandati et al. [37] have deposited CIGS alloys on Mo-sputtered glass substrate by sequential pulsed electrodeposition method, and by using Mott–Schottky, they established that the film is p-type conductivity and have carrier density around 2.6×10^{16} cm^{-3}.

Furthermore, we can estimate L_{D} the Debye screening distance, and W_{D} the thickness of depletion region from both N_A density of donors, and V_{fb} flat band potentials, respectively. The following equations give both L_{D} and W_{D} [38]:

$$L_{\mathrm{D}} = \left(\frac{\varepsilon\varepsilon_0 kT}{e^2 N}\right)^{\frac{1}{2}} \tag{7}$$

$$W_{\mathrm{D}} = \left(\frac{2\varepsilon\varepsilon_0}{eN}\right)^{\frac{1}{2}}\left(V - V_{\mathrm{fb}} - \frac{kT}{e}\right) \tag{8}$$

Both W_{D} and L_{D}, corresponding to $V - V_{\mathrm{fb}} = 1$ V, are collected in Table 4. This larger depletion region is tremendous for dissociation of the charge carriers. The prejudice of the Mott–Schottky curve did not modify considerably, signifying that the composition of the CIGS film is approximately uniform over its depth.

4 Conclusion

In this paper, we synthesized CIGS thin films by using a single-step electrodeposition process. X-ray diffraction patterns reveal the chalcopyrite phase of the fabricated CIGS thin films. We found that better quality films are achieved at optimal annealing temperature 350 °C. EDS measurement also affirms that the alloys deposited at 350 °C with 20.57 at.% Cu, 14.53 at.% In, 6.25 at.% Ga, and 39.19 at.%Se the appropriate chemical composition for

application in photovoltaic devices. UV–Vis–NIR measurements show that alloys have optical band gap ranges from 1.12 to 1.33 eV depending upon the Ga/(Ga + In) ratio. Electrochemical impedance data were performed at various Ga/(Ga + In) ratios to establish the film capacitance. By Mott–Schottky plots, we confirmed the p-type conductivity of the CIGS film, the charge carrier density about of 10^{16} cm^{-3}, a flat band potential V_{fb} ranging from −0.49 to −0.37 V, and the thickness of the depletion region between 0.24 and 0.36 μm.

Acknowledgments This work was financially supported by the Centre of Research and Technology of Energy, Technopole of Borj Cedria. Tunisia.

References

1. P. Jackson, D. Hariskos, R. Wuerz, O. Kiowski, A. Bauer, T. Friedlmeier, M. Powalla, Phys. Status Solidi RRL **9**, 28–31 (2015)
2. T. Tanaka, Y. Demizu, A. Yoshida, J. Appl. Phys. **81**, 7619 (1997)
3. R.C. Valderrama, P.J. Sebastian, J. Pantoja Enriquez, S.A. Gamboa, Sol. Energy Mater. Sol. Cells **88**, 145–155 (2005)
4. M. Nie, K. Elmer, Thin Solid Films **536**, 172 (2013)
5. D.Y. Lee, S. Park, J. Ho Kim, Curr. Appl. Phys. **11**, S88–S92 (2011)
6. C. Mahendran, N. Suriyanarayanan, Phys. B **408**, 62 (2013)
7. A. Kampmann, V. Sittinger, J. Rechid, Thin Solid Films **361–362**, 309–313 (2000)
8. V.K. Kapur, A. Bansal, P. Le, O.I. Asensio, Thin Solid Films **431–432**, 53–57 (2003)
9. M.G. Faraj, K. Ibrahim, A. Salhin, Mater. Sci. Semicond. Process. **15**, 206–213 (2012)
10. P. Luo, C. Zhu, G. Jiang, Solid State Commun. **146**, 57 (2008)
11. C. Guillen, J. Herrero, Vacuum **67**, 659 (2002)
12. M.E. Calixto, K.D. Dobson, B.E. McCandless, R.W. Birkmire, J. Electrochem. Soc. **153**, G521 (2006)
13. M. Itagaki, K. Hoshino, I. Shitanda, K. Watanabe, J. Power Sources **195**, 6905 (2010)
14. M. Itagaki, Y. Nakano, I. Shitanda, K. Watanabe, Electrochim. Acta **56**, 7975–7983 (2011)
15. R.K. Panda, D. Behera, J. Alloys Compd. **587**, 481–486 (2014)
16. A.M. Van Wezemael, W.H. Laflere, F. Cardon, W.P. Gomes, J. Electroanal. Chem. **87**, 105–109 (1978)
17. P. Herrasti, E. Fatas, J. Herrero, J. Ortega, Electrochim. Acta **35**, 345–349 (1990)
18. R. Ohara, C. Lan, C. Hwang, J. Alloys Compd. **580**, S368–S372 (2013)
19. R.C. Valderrama, P.J. Sebastián, M. Miranda-Hernandez, J.P. Enriquez, S.A. Gamboa, J. Photochem. Photobiol. A Chem. **168**, 75–80 (2004)
20. R.N. Bhattacharya, A.M. Fernandez, Sol. Energy Mater. Sol. Cells **76**, 331 (2003)
21. S. Aksu, J. Wang, B. Basol, Electrochem. Solid State Lett. **12**, 33 (2009)
22. L. Ribeaucourt, G. Savidand, D. Lincot, E. Chassaing, Electrochim. Acta **56**, 6628–6637 (2011)
23. I. Horcas, R. Fernandez, J.M. Gomez-Rodriguez, J. Colchero, J. Gomez-Herrero, A.M. Baro, WSXM: software for scanning probe microscopy and a tool for nanotechnology. Sci. Instrum. **78**, 013705 (2007)
24. M. Venkatachalam, D. Kannan, S. Jayakumar, R. Balasundaraprabhu, N. Muthukumarasamy, Thin Solid Films **516**, 6848–6852 (2008)
25. G. Hanna, A. Jasenek, U. Rau, H.W. Schock, Phys. Status Solidi **179**, R7–R8 (2000)
26. G. Oskam, D. Vanmaekelbergh, J.J. Kelly, J. Electroanal. Chem. **315**, 65–85 (1991)
27. E.C. Dutoit, R.L. Van Meirhaeghe, F. Cardon, W.P. Gomes, Phys. Chem. **79**, 1206–1213 (1975)
28. L. Zhang, F-f Liu, F-y Li, Q. He, B-z Li, C-j Li, Sol. Energy Mater. Sol. Cells **99**, 356–361 (2012)
29. Y.B. Wang, R.K. Yuan, M. Wilander, Appl. Phys. A Mater. Sci. Semicond. Process. **63**, 481–486 (1996)
30. A. Lasia, in *Electrochemical Impedance Spectroscopy and Its Applications*, ed. by B.E. Conway, J. Bockris, R. White. Modern Aspects of Electrochemistry, vol 32 (Kluwer Academic/Plenum Publishers, New York, 1999), pp. 143–248
31. J.-B. Jorcin, M.E. Orazem, N. Pébère, B. Tribollet, Electrochim. Acta **51**, 1473–1479 (2006)
32. W.P. Gomes, F. Cardon, Prog. Surf. Sci. **12**, 155–216 (1982)
33. W.P. Gomes, D. Vanmaekelbergh, Electrochim. Acta **41**, 967–973 (1996)
34. Z. Mixue, W. Aixiang, L. Jun, Y. Zhiqiang, Z. Yu, Chem. J. Chin. Univ. **35**, 2310–2316 (2014)
35. M. Gloeckler (Colorado State University, Fort Collins Colorado, 2003)
36. G.-T. Pan, M.-H. Lai, R.-C. Juang, T.-W. Chung, T.C.-K. Yang, Sol. Energy Mater. Sol. Cells **94**, 1790–1796 (2010)
37. S. Mandati, B.V. Sarada, S.R. Dey, S.V. Joshi, J. Power Sources **273**, 149–157 (2015)
38. H. Wang, L. Pilon, Electrochim. Acta **63**, 55–63 (2012)